Rational Selection of Sodium Layered Oxides for High Performance Na-Ion Batteries: P2 vs O3 vs P2-O3 Intergrowths

Elisa Grépin, Ivan Moiseev, Artem Abakumov, Jean-Marie Tarascon, Sathiya Mariyappan

Rational selection of sodium layered oxides for high performance Na-ion batteries: P2 vs O3 vs P2-O3 intergrowths

Elisa Grépin,[1,2,3] Ivan A. Moiseev,[4] Artem M. Abakumov,[4] Jean-Marie Tarascon[1,2,3,*] and Sathiya Mariyappan[1,3,**]

[1]Chimie du Solide-Energie, UMR 8260, Collège de France, 75231 Paris Cedex 05, France
[2]Sorbonne Université, 4 Place Jussieu, 75005, Paris, France
[3]Réseau sur le Stockage Electrochimique de l'Energie (RS2E), FR CNRS 3459, France
[4]Center for Energy Science and Technology, Skolkovo Institute of Science and Technology, 3 Nobel Street, Moscow, 121205, Russia

*Correspondence: jean-marie.tarascon@college-de-france.fr
**Correspondence: sathiya.mariyappan@college-de-france.fr

ABSTRACT

Sodium ion batteries (NIBs) are gaining importance as an energy storage technology complementary to the Li-ion batteries. In this regard, sodium-based layered oxides are recognized as one of the most suitable positive electrode candidate for NIBs, but vast variety of their chemical compositions and crystal structures complicates the selection of the best material. To shed light on different figures of merit that control the selection of layered oxide material for NIB applications, we compare here a P2, P2-O3 intergrowth and two O3 sodium layered oxides composed of the same transition metals (Ni, Mn, Ti and Zn) but in differing stoichiometries. The results show that the new P2-type $Na_{0.67}Ni_{0.3}Zn_{0.03}Mn_{0.52}Ti_{0.15}O_2$ phase reported here combines most of the advantages, such as stability towards moisture, reduced surface reactivity, better thermal stability and high rate capability, which are essential for commercialization, except for a limited capacity (~125 mAh/g) compared to the O3 $NaNi_{0.45}Zn_{0.05}Mn_{0.4}Ti_{0.1}O_2$ phase (~180 mAh/g), reported by our group previously. Altogether, this work enlarges the family of attractive Na-based positive electrodes and teaches us that we should not solely be obsessed with the capacity of a material to decide of its applicability.

Key words

Sodium ion batteries, sodium layered oxides, P-type and O-type structures, cycling stability, surface reactivity.

INTRODUCTION

With the tremendous interest in Na-ion battery (NIB) over the last decades, the NIB technology has never been this close to commercialization. With greater availability of Na and its lower cost, NIBs appear as a great contender to the ubiquitous Li-ion technology despite its inherently lower energy density. [1], [2] For a positive electrode (cathode), there are three different Na-ion chemistries in exploration, namely, (i) polyanionic materials (eg. $Na_3V_2(PO_4)_2F_3$, $NaVPO_4F$, etc), (ii) layered sodium transition metal oxide (Na_xMO_2, x is ≤ 1 and M is transition metal ion(s)) or (iii) Prussian blue analogs (PBAs). [3]–[6] Among these chemistries, sodium layered oxides are privileged for high volumetric energy and low cost applications. [7] Several sodium layered oxides that crystallize in either O-type (O3, O1 with O3 as majority) or P-type (P2, P3 with majority of P2 phases) structures are reported in the literature with a variety of the transition metals involved. In the O-type and P-type structures, sodium resides in octahedral and trigonal prismatic sites, respectively. This, along with the difference in layer stacking modes in the O3, O1, P2 and P3 structures, alters the electrochemical performance of the resulting materials. [8] The stoichiometric O3 sodium layered oxides with 1 Na per one transition metal cation are reported as preferably high capacity electrodes. In contrast, the P2 sodium layered oxides, with less Na per one transition metal cation (i.e. Na-deficient) have a lower capacity but are better regarding high rate capability. [9] However, capacity and rate capability are not the only key factors for successful commercial application; many other parameters need to be considered to ensure the practicality of the material. Of paramount importance is the proper choice of the cations to rule the competition between the O3 and P2 structures, as well as the structural stability during cycling. Bearing this in mind, we have investigated the Na_xMO_2 layered oxides with four M cations (Ni^{2+}, Zn^{2+}, Mn^{4+} and Ti^{4+}) for the following reasons based on our previous

report. [10] Ni participates in the redox process ($Ni^{2+/4+}$), while Mn^{4+} and Ti^{4+} stabilize the structure by suppressing the cooperative Jahn-Teller distortion of Ni^{3+} during cycling. [11] Zn^{2+} helps in stabilizing the structure in highly de-sodiated state by being redox inactive, hence reducing the amount of Na^{+} that could be removed from the structure during oxidation at high voltages. [10], [12] The transition metal stoichiometry is then tuned in such a way to synthesize pure P2, P2/O3 or O3 type materials. [13] As a result of this rational design, two new compositions namely P2 $Na_{0.67}Ni_{0.3}Zn_{0.03}Mn_{0.52}Ti_{0.15}O_2$ and P2/O3 intergrowth $Na_{0.76}Ni_{0.35}Zn_{0.03}Mn_{0.52}Ti_{0.1}O_2$ were prepared and their electrochemical performances were compared to O3 $Na_{0.9}Ni_{0.4}Zn_{0.05}Mn_{0.4}Ti_{0.15}O_2$ and O3 $NaNi_{0.45}Zn_{0.05}Mn_{0.4}Ti_{0.1}O_2$ phases reported previously.

Such a comparison was made in terms of energy density, structural and electrochemical stability vs. Na^{+}/Na^{0}, cycle life and rate capabilities as well as in terms of thermal and moisture stability. First, all the four materials show nearly similar cycling stability (>90% after 100 cycles) indicating the structural stability during cycling is mainly controlled by the transition metals involved. Secondly, the P2 phase, despite its lower capacity, displays an edge over with respect to practicality, as it is more stable in moist air, hence allowing easy processing, as well as reduced surface reactivity, better thermal stability and high rate capability.

EXPERIMENTAL SECTION

Synthesis:

All sodium layered oxides were synthesized using solid-state synthesis where the stoichiometric amounts of Na_2CO_3 (Sigma Aldrich), NiO (Sigma Aldrich), Mn_2O_3 (Sigma Aldrich), ZnO (Sigma Aldrich) and TiO_2 (Sigma Aldrich) were ball milled together for 1h using

SPEX ball mill, with powder to ball ratio of 1:10. The mixed powders were calcined at 900°C for 12h followed by intermediate grinding and reheating at 1000°C for 12h, with heating and cooling rates of 3°C/min and 1°C/min respectively. The as prepared materials were always stored in an argon-filled glovebox in order to avoid their reaction with air/ moisture.

Material and electrochemical characterization:

The phase purity and structural analyses of the samples were deduced from X-ray powder diffraction (XRD) using BRUKER D8 Advance diffractometer equipped with Cu K_α radiation source ($\lambda K_{\alpha1}$ = 1.54056 Å, $\lambda K_{\alpha2}$ = 1.54439 Å) and Lynxeye XE detector from 10 to 70°. Fullprof program was used to perform Rietveld refinements.[14] Structural evolutions during electrochemical cycling were followed by operando XRD analysis with a homemade operando XRD cell using Be window as a current collector as explained elsewhere. [15]

The reactivity of the powders against moisture was determined by placing the samples in a desiccator with a saturated $Mg(NO_3)_2$ solution to have a controlled atmosphere with humidity of ≈55% RH. The water content was determined by thermogravimetric analysis using a Mettler Toledo TGA/DSC3+LF/1100 from ambient temperature to 850°C. The thermal stability of the oxidized samples were analysed by TGA/DSC by placing ~5 mg of the sample charged to 4.5V in an aluminum crucible with or without electrolyte. The Al pan was heated at a rate of 5°C/min under an argon flow of 50 mL/min from 25°C to 300°C.

Electrochemical tests were carried out in Swagelok-type Na-metal half-cells using metallic sodium as a counter electrode and in CR2032 coin type Na-ion full cells using hard carbon coated on Al foil (12mm circular discs with a loading of 5mg/cm^2, dried at 80°C for 12h under vacuum) as negative electrode. The composite positive electrode was fabricated by ball milling in a SPEX-8000 for 30 minutes Na-based phases with super P carbon (wt% 85-15),

with a powder to bead ratio of 1:25. Whatman GF/D borosilicate glass fiber separators soaked into a 1M $NaPF_6$ in propylene carbonate (PC) solvent as electrolyte were used as separators. The assembled cells were cycled at C/10 rate (1C is the capacity corresponding to removing one sodium) within the voltage window of 2.2 - 4.5 V for half-cells and 1.2- 4.4 V for full cells, using Bio-Logic (France) potentiostat/galvanostat. Rate capability tests were carried out by charging the material to 4.5V at C/10 then discharging successively at 5C, 2C, 1C, C/2, C/5, C/10 and C/20 with a 4h rest between each step. [16] Lastly, galvanostatic intermittent titration technique (GITT) was performed in Swagelok–type cells with 1h pulses at C/20 and 6h rest periods. [17]

For transition metal dissolution study, charged samples of P2 and O3 materials were kept in 1M $NaPF_6$ in EC-PC-DMC (1:1:2 by weight) solution at 55°C for 2 weeks and the supernatant liquid was filtered using a 0.2 µm syringe and analyzed using Inductively Coupled Plasma Mass Spectrometry (ICP-MS) for their transition metal ion content. [18] The electrolyte containing DMC is used solely for this transition metal dissolution study alone as it was reported that the parasitic reactions are more pronounced with the linear carbonate containing electrolytes. [19]

Samples for transmission electron microscopy (TEM) studies were prepared in an Ar-filled glovebox by crushing the crystals with an agate mortar and pestle under dimethyl carbonate (DMC) and depositing a drop of suspension onto a carbon film supported by a copper grid. Vacuum transfer holder was used to transfer sample from glovebox to microscope column avoiding contact with air and moisture. High angle annular dark field scanning transmission electron microscopy (HAADF-STEM) images as well as selected area electron diffraction (SAED) patterns and energy-dispersive X-ray (EDX) maps were acquired on a Titan Themis Z

transmission electron microscope at 200 kV equipped with a Super-X system for EDX analysis.

RESULTS AND DISCUSSIONS:

Design and Synthesis of sodium layered oxide with P2, O3 and P2/O3 intergrowth structures:

To design sodium layered oxides having same transition metal ions but crystallizing in different structures (P2 or O3), calculations of cationic potential were used, as reported by Zhao *et al*. [13] At the beginning, transition metal stoichiometry composition was kept constant (0.45Ni, 0.05Zn, 0.4Mn and 0.1Ti) and sodium content was reduced. Calculations found (Figure 1a) that for sodium contents ranging from 0.7 to 1, the most stable form is the O3 phase.

To cross check our calculation results, these compositions were synthesized by milling stoichiometric quantities of the precursors together and calcining at high temperature (1000 °C), followed by slow cooling to stabilize the thermodynamically most stable structure for each composition. The XRD patterns of the resultant compounds exhibit O3 structure for 0.8, 0.9 and 1Na content while a mixture of O3 and P2 phases is obtained for 0.7Na as seen in Figure 1b, hence contradicting our calculations. In addition, all the materials show cubic metal oxide (NiO) impurities that increase with decreasing amount of sodium content, highlighting the difficulty to control the final product due to partial decomposition of the formed product at high temperature. By decreasing Na-stoichiometry, the material require Ni^{3+} to compensate the charge balance; since Ni^{3+} is less stable in the MO_2 layer, it leads to its expulsion as NiO. [20]

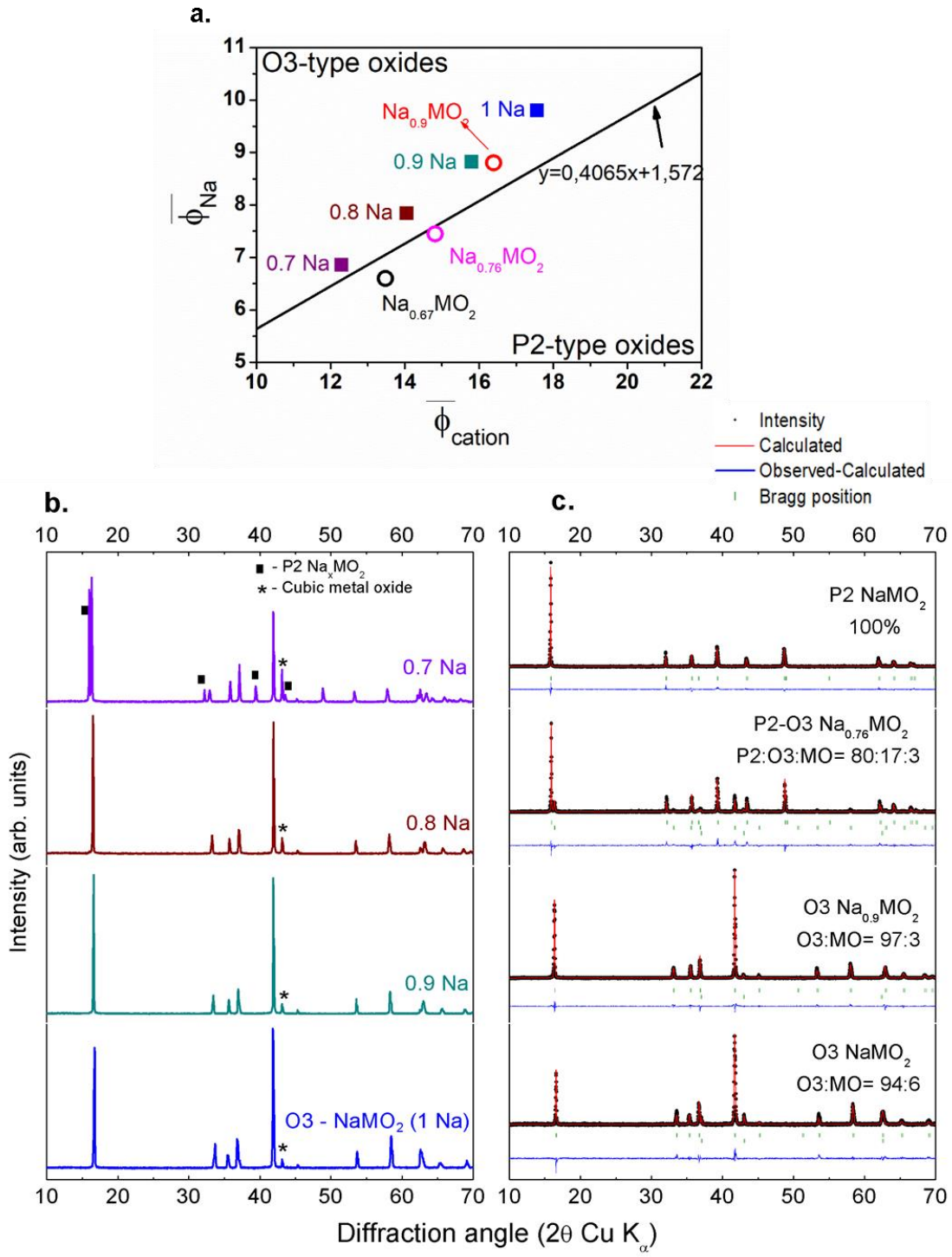

Figure 1: a) Cationic potential of the different materials considering the Na content, oxidation state and composition of transition metals. b) Powder XRD patterns of the synthesized materials with different sodium stoichiometry but with the same transition metals stoichiometry (0.45Ni, 0.05Zn, 0.4Mn, 0.1Ti). c) Rietveld refinements of the four compounds with modified transition metal compositions: $Na_{0.67}Ni_{0.3}Zn_{0.03}Mn_{0.52}Ti_{0.15}O_2$ ($Na_{0.67}MO_2$), $Na_{0.76}Ni_{0.35}Zn_{0.03}Mn_{0.52}Ti_{0.1}O_2$ ($Na_{0.76}MO_2$), $Na_{0.9}Ni_{0.4}Zn_{0.05}Mn_{0.4}Ti_{0.15}O_2$ ($Na_{0.9}MO_2$) and $NaNi_{0.45}Zn_{0.05}Mn_{0.4}Ti_{0.1}O_2$ ($NaMO_2$). The O3, P2 and metal oxide (MO) phases are refined using the space group *R*-3*m*, *P*6$_3$/*mmc* and *Fm*-3*m*, respectively. See supporting tables S1 to S3 for the refined parameters.

Next, the transition metal compositions were modified such that the total charge in the final material is maintained by having Ni, Zn, Mn and Ti in their most stable oxidation state of +2, +2, +4 and +4, respectively. The charge on the transition metal ions is then balanced together with the sodium content for it to be +4. Based on this reasoning, the four compositions $Na_{0.67}Ni_{0.3}Zn_{0.03}Mn_{0.52}Ti_{0.15}O_2$ ($Na_{0.67}MO_2$), $Na_{0.76}Ni_{0.35}Zn_{0.03}Mn_{0.52}Ti_{0.1}O_2$ ($Na_{0.76}MO_2$), $Na_{0.9}Ni_{0.4}Zn_{0.05}Mn_{0.4}Ti_{0.15}O_2$ ($Na_{0.9}MO_2$) and $NaNi_{0.45}Zn_{0.05}Mn_{0.4}Ti_{0.1}O_2$ ($NaMO_2$) were virtually designed and the cationic potential calculations predict an O3 stacking for $Na_{0.9}MO_2$ and $NaMO_2$ and a P2 one for $Na_{0.67}MO_2$ and $Na_{0.76}MO_2$ as shown in Figure 1a by circles. These compositions were synthesized by solid state synthesis as explained above and the XRD powder patterns of the resulting samples are reported in Figure 1c.

Rietveld refinements show that $Na_{0.67}MO_2$ adopts the P2 stacking, in agreement with our calculation, with lattice parameters a = 2.90319 (3) and c = 11.16876 (2) Å. Similarly, $NaMO_2$ and $Na_{0.9}MO_2$ are stabilized in the O3 phase as expected from Figure 1a with the following lattice parameters of a = 2.96779 (4) and c = 16.0245 (4) Å and a = 2.95220 (2) and c = 16.21777 (3) Å, respectively. The increase in c-parameter while moving from $NaMO_2$ to $Na_{0.9}MO_2$ can be linked to its lesser sodium content hence the increased repulsion between the MO_2 layers due to reduced screening by Na^+ ions. A cubic metal oxide impurity phase (Zn-substituted NiO) is observed for both O3 phases, however its content is lower for $Na_{0.9}MO_2$ (~3 wt%) than that for $NaMO_2$ (~6 wt%). Nonetheless, for the $Na_{0.76}MO_2$ composition, the XRD pattern shows peaks due to both P2 and O3 structures instead of P2 as predicted in Fig. 1a. Its structure has been refined to be ~17wt% in R-3m space group with a = 2.95106 (9) and c = 16.22521 (99) Å, and ~80wt% in $P6_3/mmc$ with a = 2.90293 (3) and c = 11.12897 (22) Å. It once again indicates the challenges in synthesizing the sodium layered oxide in a specific structure as stoichiometry and synthesis conditions play a major role in

determining the final phase. Finally, $Na_{0.76}MO_2$ also exhibits small amount (less than 3 wt. %) of cubic metal oxide impurity. At this stage, since the O3 phases were previously studied by our group, [10] the further analyses on structure and Na-insertion properties are focused solely on P2 $Na_{0.67}MO_2$ and P2/O3 $Na_{0.76}MO_2$ phases before comparing them with O3 phases for their application in Na-ion batteries.

P2 $Na_{0.67}Ni_{0.3}Zn_{0.03}Mn_{0.52}Ti_{0.15}O_2$ (P2 - $Na_{0.67}MO_2$) :

The electrochemical performance of P2 $Na_{0.67}Ni_{0.3}Zn_{0.03}Mn_{0.52}Ti_{0.15}O_2$ was tested in sodium half cells using sodium metal as counter electrode. For comparative purpose, the cycling performance of Zn and Ti-unsubstituted P2 $Na_{0.67}Ni_{0.33}Mn_{0.67}O_2$, Ti-substituted P2 $Na_{0.67}Ni_{0.33}Mn_{0.52}Ti_{0.15}O_2$ and Zn-substituted P2 $Na_{0.67}Ni_{0.3}Zn_{0.03}Mn_{0.67}O_2$ were also carried out (XRD patterns of the prepared material reported in Fig S1) in the same condition and the cycling profiles are shown in Fig. 2a, with their corresponding derivative plots in Figure 2b. The Zn, Ti unsubstituted P2 $Na_{0.67}Ni_{0.33}Mn_{0.67}O_2$ exhibits 3 well-defined plateaus during cycling together with a sharp redox peak (in the derivative plot Fig. 2b) around ~4.2V indicating a biphasic process. In turn, for the Zn^{2+}, Ti^{4+} substituted materials, the redox process >4V reduces in length and gets broadened showing a change in the redox behavior of these materials.

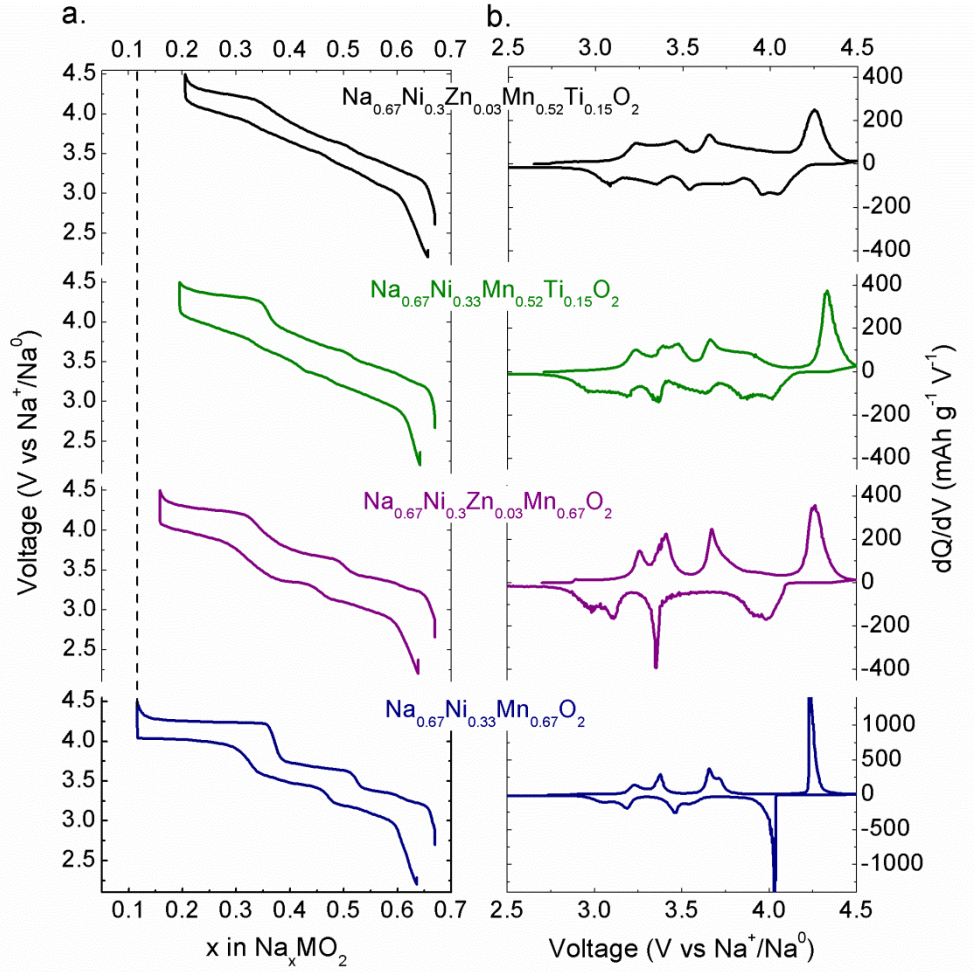

Figure 2: a) Galvanostatic charge/discharge curves of P2 $Na_{0.67}Ni_{0.3}Zn_{0.03}Mn_{0.52}Ti_{0.15}O_2$, P2 $Na_{0.67}Ni_{0.33}Mn_{0.67}O_2$, $Na_{0.67}Ni_{0.3}Zn_{0.03}Mn_{0.67}O_2$ and $Na_{0.67}Ni_{0.33}Mn_{0.52}Ti_{0.15}O_2$, versus metallic sodium at C/10 between 2.2 – 4.5 V. b) their corresponding derivative plots.

Similar shortening of high voltage plateau and broadening of the peaks in the derivative plots is also observed while replacing Zn^{2+} with Cu^{2+} or Mg^{2+} (Supporting Fig. S2 and S3). To interrogate the origin of such changes in the cycling profile by Zn, Ti co-substitution, the structural evolutions of P2 $Na_{0.67}Ni_{0.3}Zn_{0.03}Mn_{0.52}Ti_{0.15}O_2$ were analyzed by operando XRD and compared them with the Zn, Ti unsubstituted material P2 $Na_{0.67}Ni_{0.33}Mn_{0.67}O_2$ (Figure 3).

The XRD evolution of P2 $Na_{0.67}Ni_{0.3}Zn_{0.03}Mn_{0.52}Ti_{0.15}O_2$ in Figure 3a shows no biphasic regions during cycling, but rather a continuous change in the *c* lattice parameter with the increase at the beginning of the cycle and contraction as the material approaches complete desodiation

(above 3.8 V, < 0.33 Na in the structure). It differs from the P2 $Na_{0.67}Ni_{0.33}Mn_{0.67}O_2$ (Figure 3b) which shows well-defined bi-phasic regions with the appearance of secondary O2 phase nearing the end of charge (for x<1/3 in $Na_xNi_{0.33}Mn_{0.67}O_2$) that induces high volume changes during the cycling, which is detrimental to the structural stability. [21] Instead, fully charged P2 $Na_{0.67}Ni_{0.3}Zn_{0.03}Mn_{0.52}Ti_{0.15}O_2$ is quite similar to the widely reported OP4 phase with O2-P2 intergrowths. Such OP4 phase formation is associated with lesser volume change from the pristine P2 phase, in comparison to the O2 phase formation for the Zn, Ti-unsubstituted $Na_{2/3}Ni_{0.33}Mn_{0.67}O_2$. [22] On subsequent discharge, the process is fully reversible as observed by nearly the same lattice parameters at the beginning and at the end of the cycle (a = 2.9027 (8) Å and c = 11.169 (3) Å).

It is important to note that similarly, phase transitions with smaller volume changes are observed upon Zn, Ti co-substitution in O3 $NaNi_{0.5}Mn_{0.5}O_2$ material, pointing out its structure stabilizing effect, with the resultant O3 $NaNi_{0.5-y}Zn_yMn_{0.5-z}Ti_zO_2$ exhibiting better long term cycling stability.

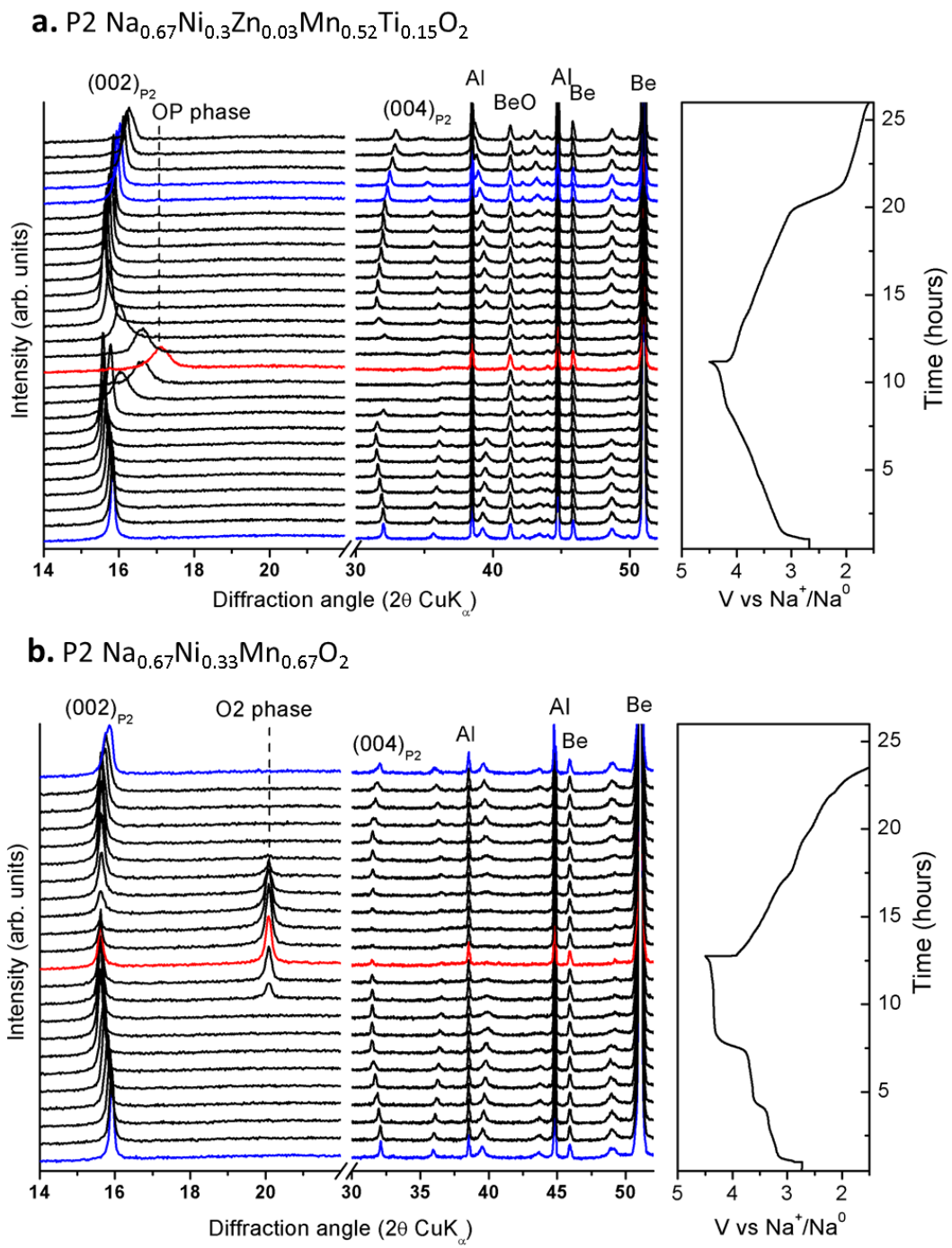

Figure 3: Operando XRD analysis of P2 $Na_{0.67}Ni_{0.3}Zn_{0.03}Mn_{0.52}Ti_{0.15}O_2$ (a) and P2 $Na_{0.67}Ni_{0.33}Mn_{0.67}O_2$ (b) versus metallic sodium at C/20 between 1.5 – 4.5 V. Note that the (002) and (004) peaks shift to lower angle in the initial stages of oxidation due to the decrease in *c* parameter by the removal of screening Na^+ ion, and shifts back to higher angle nearing end of charge with the formation of OP4 type structure for Zn, Ti-co-substituted phase (P2 $Na_{0.67}Ni_{0.3}Zn_{0.03}Mn_{0.52}Ti_{0.15}O_2$ in a) and O2 phase formation for Zn, Ti-unsubstituted material (P2 $Na_{0.67}Ni_{0.33}Mn_{0.67}O_2$ in b). On discharge down to 1.5V, the P2 phase is preserved as seen by the absence of any peak splitting as reported for P2 to P2' phase transition. [23], [24]

P2/O3 $Na_{0.76}Ni_{0.35}Zn_{0.03}Mn_{0.52}Ti_{0.1}O_2$ (P2/O3 $Na_{0.76}MO_2$):

The XRD pattern of $Na_{0.76}MO_2$ exhibits a mixture of P2 and O3 phases (Figure 1c). For a better understanding of the segregation of these phases, high angle annular dark field scanning transmission electron microscopy (HAADF-STEM) and selected area electron diffraction (SAED) analyses were carried out. The main reflections in the SAED patterns (supporting Fig. S4) indicate hexagonal $P6_3/mmc$ structure (P2 phase with $a \approx 2.9$ Å and $c \approx 11.4$ Å). The HAADF-STEM images in Figure 4 also confirm the P2 phase in the core of the crystallites. However, a 2-4 nm shell (brighter region in Figure 4a,b) is clearly seen around the crystallite, where the interlayer distance is ~4.7Å compared to ~5.7Å in the P2 phase core. The shell demonstrates a lateral shift of the cationic layers over 1/3 of the distance between the projected cationic columns visible in the [100] HAADF-STEM image (Supporting Fig. S5) indicating *R*-3*m* O3 "cubic" close-packed structure. The core-P2 and shell-O3 phases form coherent (002)/(003) (Fig. 4b) and {112}/{012} (Fig. 4a) interfaces. At the {112}/{012} interface, the (003) planes of the O3 structure are rotated by ~33.8° with respect to the (002) planes of the P2 structure to compensate for mismatch in the interplanar spacings (Fig. 4a). Finally, the HAADF intensity profiles (supporting Fig. S6) show the absence of transition metal ions in the Na-layer for the P2 core, while significant occupation of the Na positions with the TM cations was observed in the O3 shell.

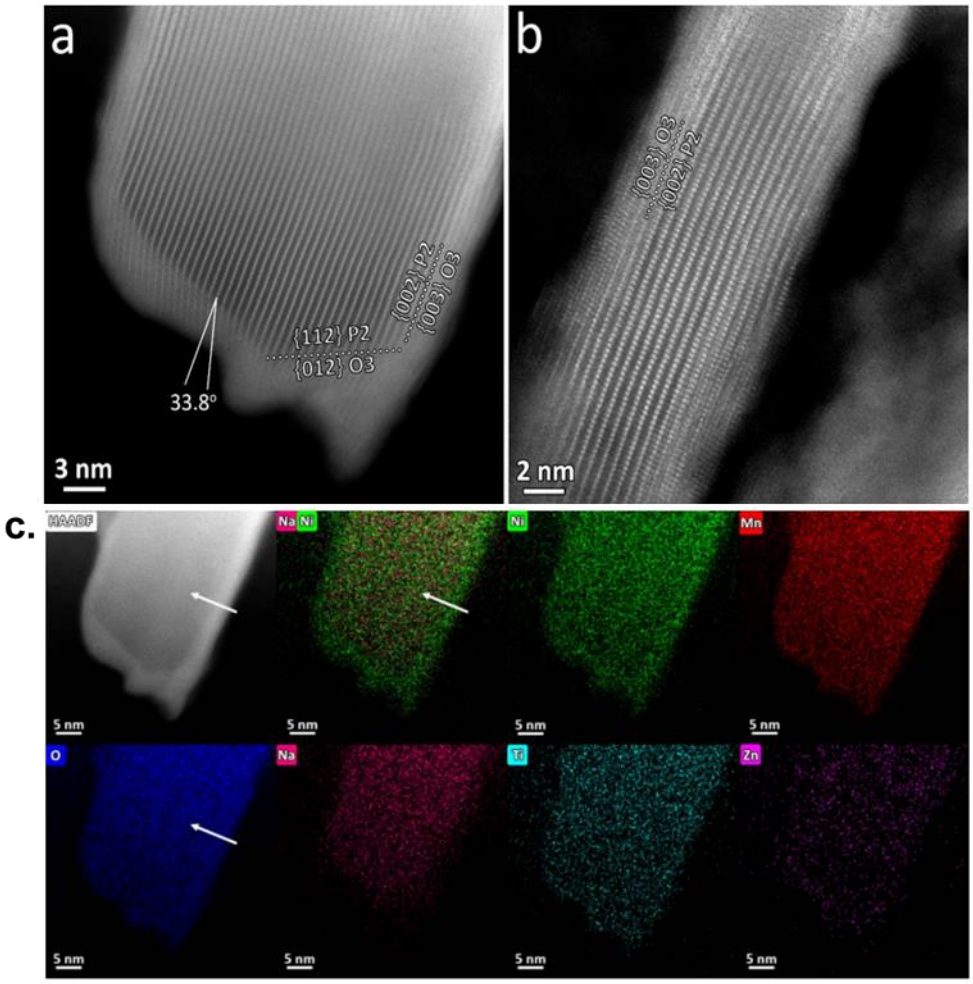

Figure 4. a) $[1\bar{1}0]$ and b) [100] HAADF-STEM images of P2/O3 $Na_{0.76}Ni_{0.35}Zn_{0.03}Mn_{0.52}Ti_{0.1}O_2$. c) HAADF-STEM image and the corresponding color-coded elemental maps and the mixed EDX map for Na and Ni. White arrows indicate the place and direction of the EDX line scan for Ni, Na, and O in SI Fig. S5.

The STEM-EDX compositional maps (Fig. 4c) demonstrate cationic distribution within the P2 and O3 phases. The O3 phase is slightly enriched with Ni and significantly depleted with Na having the Na/TM ratio of 0.25:1 (see supporting Fig S7 and Table S4). Such poor Na-stoichiometry could be in the origin of transition metal migration to the sodium layer in the O3 shell. The composition of the P2 phase in the core is $Na_{0.72}Ni_{0.33}Zn_{0.03}Mn_{0.54}Ti_{0.1}O_2$ (See Table S4 in SI for calculation) which is closer to the composition of P2 $Na_{0.67}MO_2$ reported above.

The electrochemical performance of P2/O3 $Na_{0.76}MO_2$ was tested in sodium half-cell and the obtained cycling profile is compared with the one of P2 $Na_{0.67}MO_2$ (Figure 5a, left with the corresponding derivative plots in the right). The P2/O3 $Na_{0.76}MO_2$ shows relatively higher polarization than the P2 phase, probably due to the O3 shell with significant amount of M in the Na positions blocking Na-ion diffusion paths. Next, the P2/O3 $Na_{0.76}MO_2$ intergrowths exhibits many plateaus and sloppy regions, majority of which resembles that of the P2 phase, with the extra peaks marked by arrow in the derivative plot most probably due to the O3 phase in the shell. To analyze these phase transitions further, operando XRD analysis (Figure 5b) was carried out at C/20 rate with one XRD pattern recording for every 0.05Na removal. The (003) peak of the O3-phase disappears in the initial stages of de-sodiation indicating that sodium is initially removed from the O3 phase in the shell. After the removal of ~0.1Na, all the peaks due to O3 phase disappear completely. Meanwhile, the (002) peak of the P2 phase starts to shift towards low angles (increasing the *c* parameter from MO_2 layer repulsion due to the screening Na removal) until 3.7V, after which the XRD patterns became more complex with the appearance of new peaks together with some peak shifting happening at the same time. It shows the de-sodiation mechanism at this potential is more complex involving most likely the Na-diffusion from O3/P2 or both. Finally, upon complete de-sodiation, the peaks became broad with reduced intensity indicating possible O- and P-type intergrowths as reported before. [22], [25], [26]. On discharge, the whole process is reversible as witnessed by the XRD collected at the end of the discharge at 2.5V that nearly superimpose with that of the pristine sample, implying a complete reversibility of all the phase transitions from both O3 and P2 components.

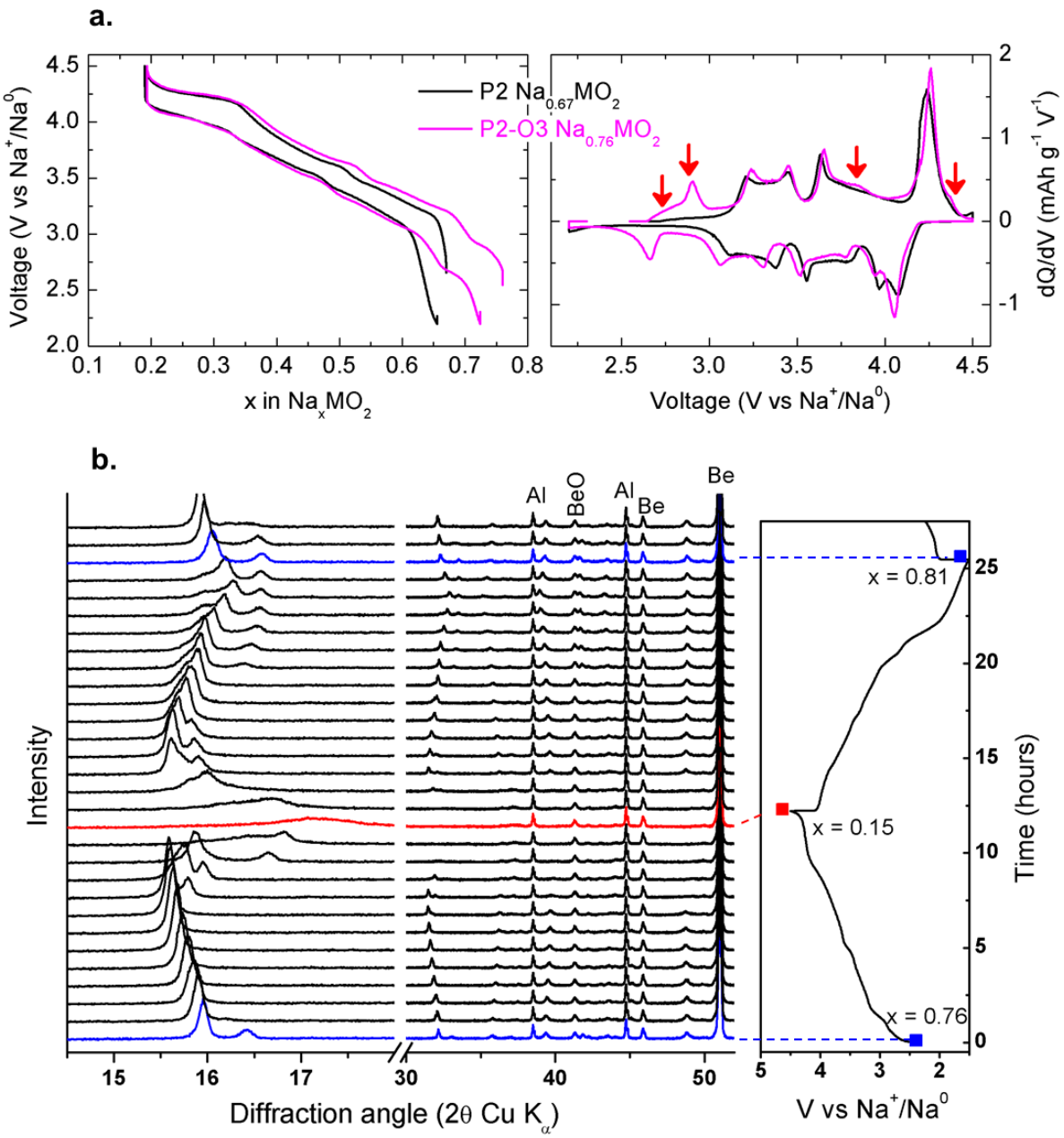

Figure 5. a) Electrochemical performance of P2-O3 $Na_{0.76}MO_2$ (pink line) in comparison with P2 $Na_{0.67}MO_2$ (black) in Na-metal half cell (left) composition vs voltage plot and (right) derivative plot of the same. (b) Operando XRD analysis of P2-O3 $Na_{0.76}MO_2$ where the cycling is carried out at C/20 rate with one XRD pattern for every one hour (0.05Na removal); (left) XRD evolution (right) corresponding galvanostatic charge- discharge cycle.

Having studied the structural and electrochemical properties of Zn, Ti co-substituted P2 $Na_{0.67}MO_2$ and P2/O3 $Na_{0.76}MO_2$ intergrowths, next their performances are compared with the O3 $Na_{0.9}MO_2$ and $NaMO_2$ for their applicability in Na-ion batteries.

Benchmarking P2 vs P2/O3 vs O3 electrodes

(i) Electrochemical properties: Na-ion full cells for all the four sodium layered oxides against hard carbon negative electrode were assembled using 1M $NaPF_6$ dissolved in propylene carbonate (PC) as electrolyte and their cycling profiles were gathered in Fig. 6a (the half-cell cycling profiles are shown in Fig. S8 for the layered oxides and in Fig. S9 for the hard carbon).

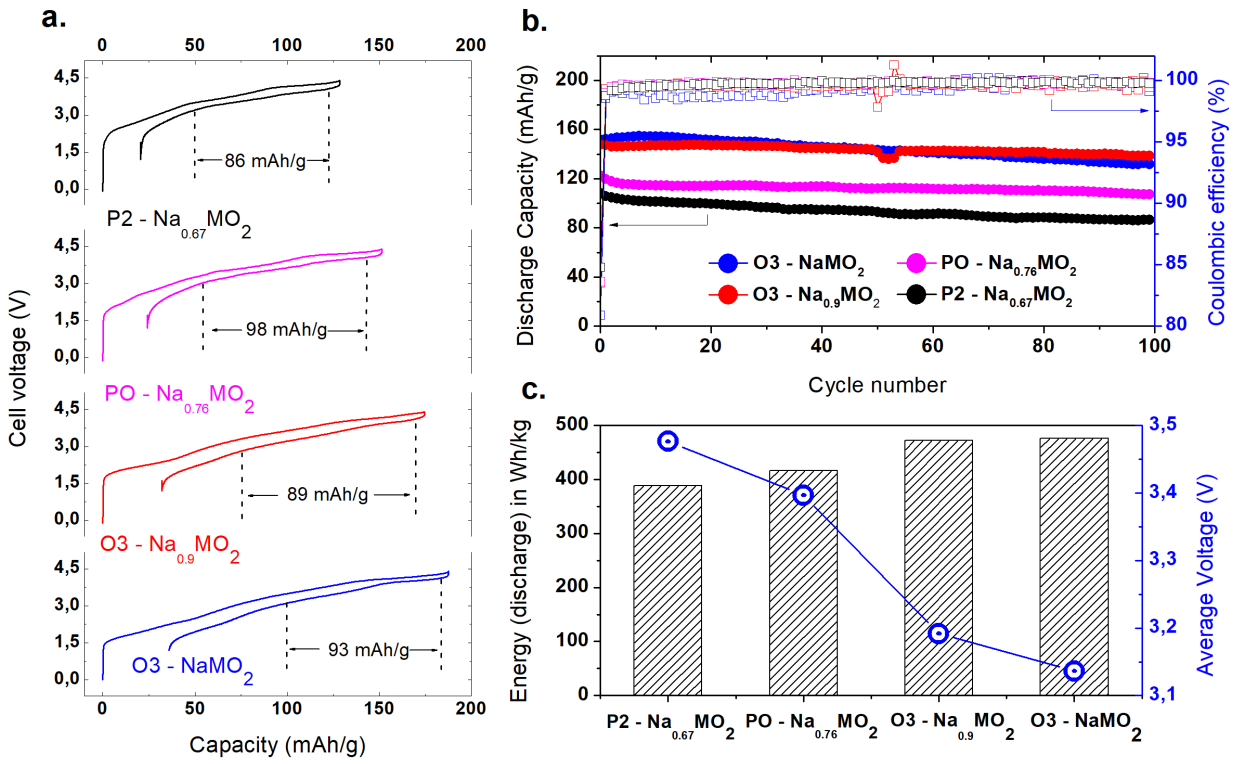

Figure 6: a) Galvanostatic charge/discharge curves of sodium layered oxides in Na-ion full cells using hard carbon negative electrode cycled between 1.2 – 4.4 V at a rate of C/10. The dotted lines in the figure is an indication for eye to show the possible capacity from each material in the reduced voltage window of 3- 4.3V, where all 4 materials show similar capacity. b) Capacity retention plot in full cells for each material. c) Comparison of the discharge energy and average voltage for each compound in the voltage range of 1.2 - 4.4 V. Energy values are normalized for the total weight of positive and negative material to have uniform comparison.

First, it should be noted that a wide voltage window of 1.2- 4.4 V is required to utilize the full capacity of the O3 phases ($Na_{0.9}MO_2$ and $NaMO_2$), while a smaller voltage window of 3- 4.3 V is sufficient to nearly achieve the full capacity of the P2 $Na_{0.67}MO_2$-HC based Na-ion cell. This

narrow voltage window is a serious asset that makes the P2 phase of interest in practical applications. All four samples exhibit nearly the same capacity retention (Figure 6b) of ~90% after 100 cycles indicating the structural stability (see Fig. S10 for curve shapes at different cycles) during cycling mainly depends on the extent of layer gliding which in turn is controlled by the transition metal ions involved.

Figure 6c shows that the highest average discharge potential is observed for P2 $Na_{0.67}MO_2$ which has the lowest capacity of the four materials studied due to the least amount of sodium in the starting structure. However, this low capacity is compensated by its high average potential, which leads to an energy density for P2 comparable to that of O3 $NaMO_2$, which has the highest capacity but lowest potential (~3.1V) among all the materials studied.

Another figure of merit regarding the practical aspects of electrode materials is their reactivity with the electrolyte that occasionally can be accompanied by transition metal dissolution due to the parasitic reaction between the electrode and electrolyte. To shed light into this phenomenon, the transition metal dissolution from the material (charged to 4.5 V) were studied by placing 20mg of P2 and O3 materials in their charged state with 2mL of 1M $NaPF_6$ in EC-PC-DMC (1:1:2 by weight) solution at 55°C for 2 weeks. Afterwards, the supernatant liquid was analyzed for the presence of transition metal ions by ICP-MS. Figure 7a shows the amount of dissolved transition metal (TM) ions together with change in XRD pattern of the charged material (supporting Fig. S11). The amount of TM dissolved from P2 $Na_{0.67}MO_2$ is much lower than that from O3 $NaMO_2$, indicating relatively smaller surface reactivity of the P2 phase with the electrolyte than the O3 material. Such surface reactivity could also influence the thermal stability of the electrode materials, which is analyzed next

by TGA-DSC. Experiments were carried out with ~5mg of the charged electrode material (4.5 V) and the TGA, DSC profiles are shown in Figure 7b and 7c, respectively.

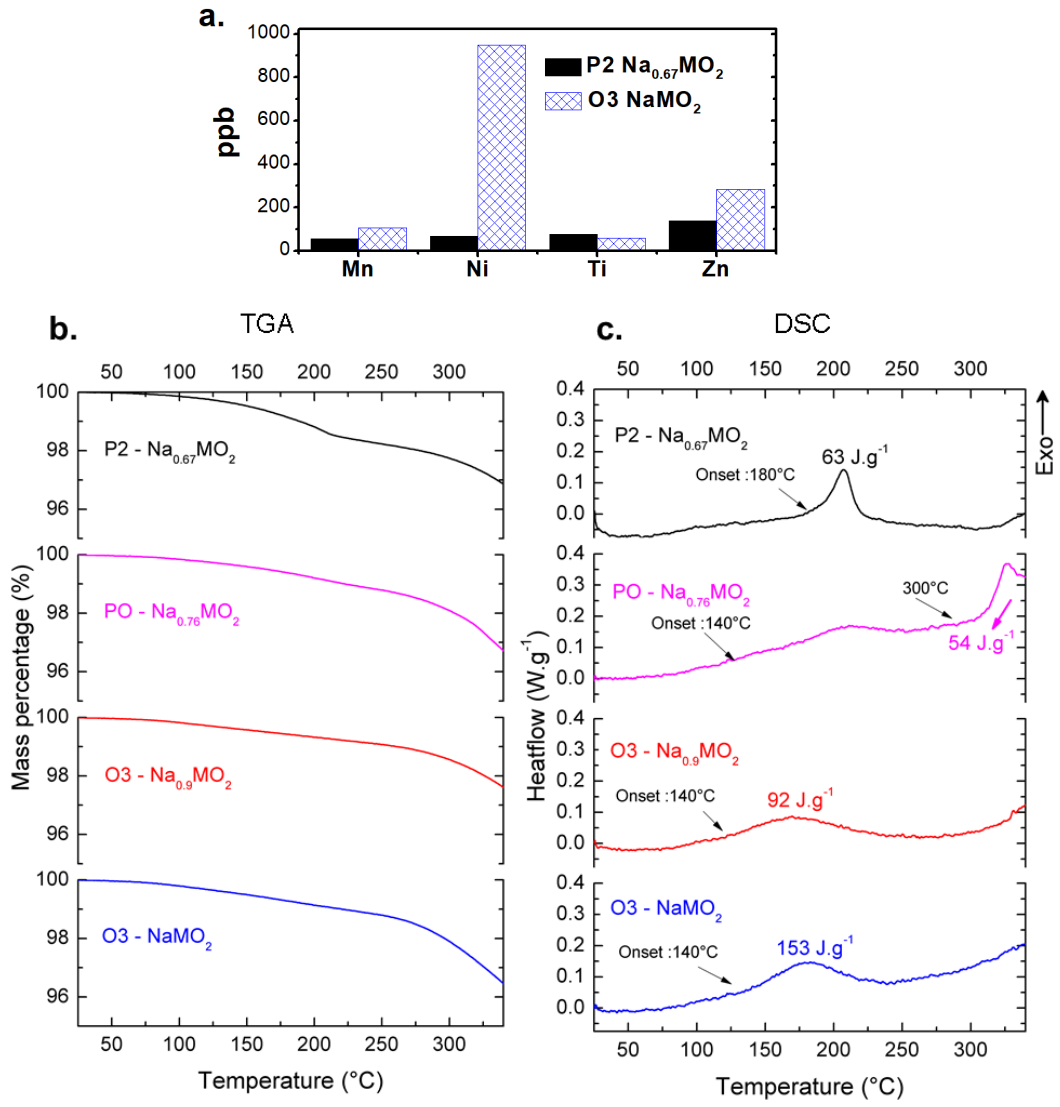

Figure 7: a) Amount of transition metal dissolved from the charged samples of P2 $Na_{0.67}MO_2$ and O3 $NaMO_2$ upon treatment with electrolyte. For the total amount of Ni, Zn, Mn, and Ti present in each material, nearly 2 wt.% of Ni, 4.8 wt.% of Zn, 0.3 wt% of Mn and 0.7 wt% of Ti were dissolved from the O3 phase, whereas 0.2 wt% of Ni, 4 wt.% of Zn, 0.1 wt.% of Mn and 0.5 wt.% of Ti were dissolved from the P2 phase. Higher value for Ti and Zn is associated with their lesser content than the Mn, Ni and hence higher error in measurement. The (b) TGA and (c) DSC of the electrode materials charged to 4.5 V. Note that the sample names are mentioned with the sodium content in the pristine material for clarity purpose, though the materials used are in their fully charged state (desodiated, 100% SOC).

All four materials showed an exothermic process where the onset temperature is relatively higher for P2 $Na_{0.67}MO_2$ (180°C) in comparison to the O3 phase (140 °C). The P2/O3

$Na_{0.76}MO_2$ phase showed the first exothermic onset around 140°C which is closer to O3 $NaMO_2$. These results confirm once again that the surface reactivity of the P2 material is lower in comparison to the O3 material and it could be related to the lesser nickel content in the P2 $Na_{0.67}MO_2$ material. Note that, the heat associated with all these materials are comparatively less than the Li-based layered oxide materials reported in the literature. [27], [28] In any case, it should be recalled that these studies were done on electrode materials lacking coatings to protect their surface and without electrolyte additives to minimize surface reactions, leaving room for further improvement in the thermal stability for real applications. It can be noted that to mimic real working conditions, thermal stability experiments (TGA/ DSC) were also done for the charged materials in presence of electrolyte, however the endothermic solvent evaporation complicates our analyses to identify the electrode materials reactivity (Supporting Fig. S12).

Altogether, the results indicate a superior performance of P2 phase due to its resistance against TM dissolution, as well as its higher thermal stability. In addition, the P2 phase also shows better rate capability with 80% of its capacity retained at 1C in comparison to solely 65% capacity retention at 1C for the O3 $NaMO_2$ material (see supporting Fig. S13- S16). However, an intrinsic weakness of the P2 phase is its limited capacity, which is slightly improved by moving to P2/O3 intergrowths. Besides all these metrics, moisture sensitivity is another critically important parameter in practical application as it affects material storage, handling and electrode processing, hence the need of evaluating it as reported next.

Moisture stability:

The moisture stability of the four sodium layered oxides were compared by exposing them to 55% RH for 3 days and checked the consequences of this treatment on the recovered

materials by XRD, TGA and electrochemical measurements. The XRD patterns in Figure 8a indicate no change in the peaks of the P2 phase (in P2 $Na_{0.67}MO_2$ and P2 component of PO $Na_{0.76}MO_2$), whereas a decrease in intensity as well as broadening of the XRD peaks of the O3 phase. No new peaks were observed at low angles ($2\theta < 14°$) indicating the absence of birnessite-like hydrated phase formation by water molecule insertion into sodium layers. [29] Instead, the O3 phase is oxidized with the loss of sodium ions from the crystal structure that react with the H_2O/ CO_2 in air to form sodium hydroxide, carbonate, hydroxycarbonate etc, that could be quantified using TGA analyses (Figure 8b) of the moisture exposed samples. [30] The mass losses around 400°C and above 600 °C are associated with decomposition of some adsorbed species (species formed due to the reaction of ejected sodium with CO_2, H_2O etc) and is the largest (nearly 8%) for O3 $NaMO_2$. P2 $Na_{0.67}MO_2$ in turn showed the least mass loss (<2%) below 200°C that is mainly due to water adsorbed on the surface of the material. Hence, from the XRD and TGA results, the moisture stability of the four sodium layered oxides studied could be ranked as P2 $Na_{0.67}MO_2$ >> PO $Na_{0.76}MO_2$ > O3 $Na_{0.9}MO_2$ > O3 $NaMO_2$, with the P2 $Na_{0.67}MO_2$ phase being the most stable towards moisture exposure. Strikingly, it is stable even while washing with water (Supporting Fig S17). Therefore, the electrode processing (coating of active material on Al current collector) for P2 material could be carried out in normal atmosphere without the need for dry room (Figure 8d right); whereas the O3 phase under similar condition (in air) leads to agglomeration, jellification of the slurry and poor quality coating (Figure 8d left).

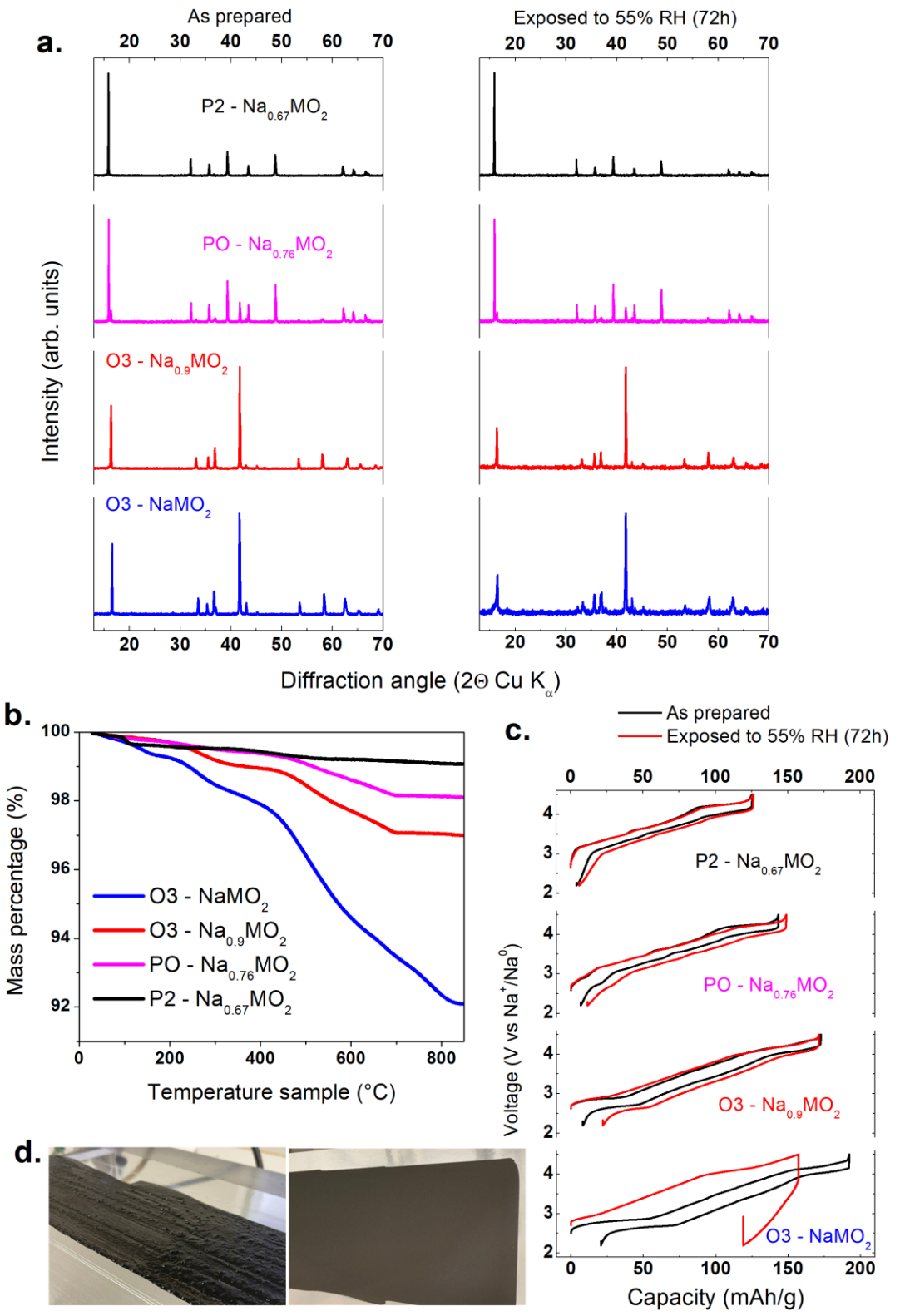

Figure 8: a) Powder XRD patterns of as prepared materials (left) in comparison to the materials after exposure to 55% RH for 72h. b) Thermogravimetric analysis of the moisture exposed materials. c) Galvanostatic charge/discharge curves in Na-metal half cells of as-prepared (black lines) and moisture exposed (red lines) materials in the voltage range of 2.2 – 4.5 V, at C/10 rate. The moisture exposed materials were dried at 100°C in vacuum before cell assembly in order to remove the absorbed water molecules on the surface. d) Picture of the jellification of an O3 slurry (left) versus non-jellified P2 slurry (right).

Furthermore, we found that exposing P2 $Na_{0.67}MO_2$ powder to moist air for a few days prior to a drying treatment (100°C in vacuum) does not affect their electrochemical performances either in Na half-cells (Figure 8c) or in Na-ion full cells (Supporting Fig. S18) which shows similar capacity retention to the cells assembled with freshly-made samples. This behavior contrasts with that of O3 powders, which crumble after being exposed to moist air and whose performances decreases rapidly upon cycling (Supporting Fig. S19) while showing a high polarization during the first cycle. Lastly, as expected, the P3-O2 intergrowths shows a milder reactivity against moisture compared to the pure O3 phase.

At this stage, an open question remains as to why the P2 phase is more stable towards moisture than the O3 phase. Several reports claim P2 phases are more sensitive to moisture due to their larger interlayer spacing, fewer Na occupancy and low energy barrier for Na^+ diffusion that can enhance the sodium removal and water insertion reactions compared to their O3 counterparts. [31], [32] However, the opposite phenomenon observed here with the P2 $Na_{0.67}MO_2$ being more stable towards oxidation by O_2 in moist air indicates the higher redox potential of P2 $Na_{0.67}MO_2$ plays a major role towards moisture stability in these materials, irrespective of the available sites for water insertion in the sodium layer.

Discussions:

The different technical and practical parameters compared so far are reunited in the spider chart (Figure 9). As a result, the P2 and O3 phases have their own advantages and disadvantages with the O3 phase having a higher sodium, a greatest capacity than the P2 phase. However, the latter has an advantage in rate capability, thermal stability and practicality (handling and processing the material). Thus, among all the studied materials, P2 $Na_{0.67}MO_2$ checks off most of the figures of merit for a successful implementation into

practical Na-ion batteries. Comparison with other reported full cell data of P2 phases can be found in Supporting Table S5 and show its competitiveness. Obvious improvements are to increase its energy density either by increasing the Na-content in the P2 phase or by designing core-shell type structures with O3 phase in the core and P2 phase in the shell. Such strategies have been explored by different groups in the literature already, where a P2 phase with nearly ~0.8 sodium was achieved by creating vacancies and substituting lithium in the metal layer. [33], [34] Similarly, core-shell structure having O3 $NaNi_{0.5}Mn_{0.5}O_2$ in the core and P2 $Na_{0.67}MnO_2$ in the shell is reported by two step wet chemical route. [35], [36] It will be interesting to further study these materials for other performance indexes discussed here in order to identify a best suitable candidate for applications.

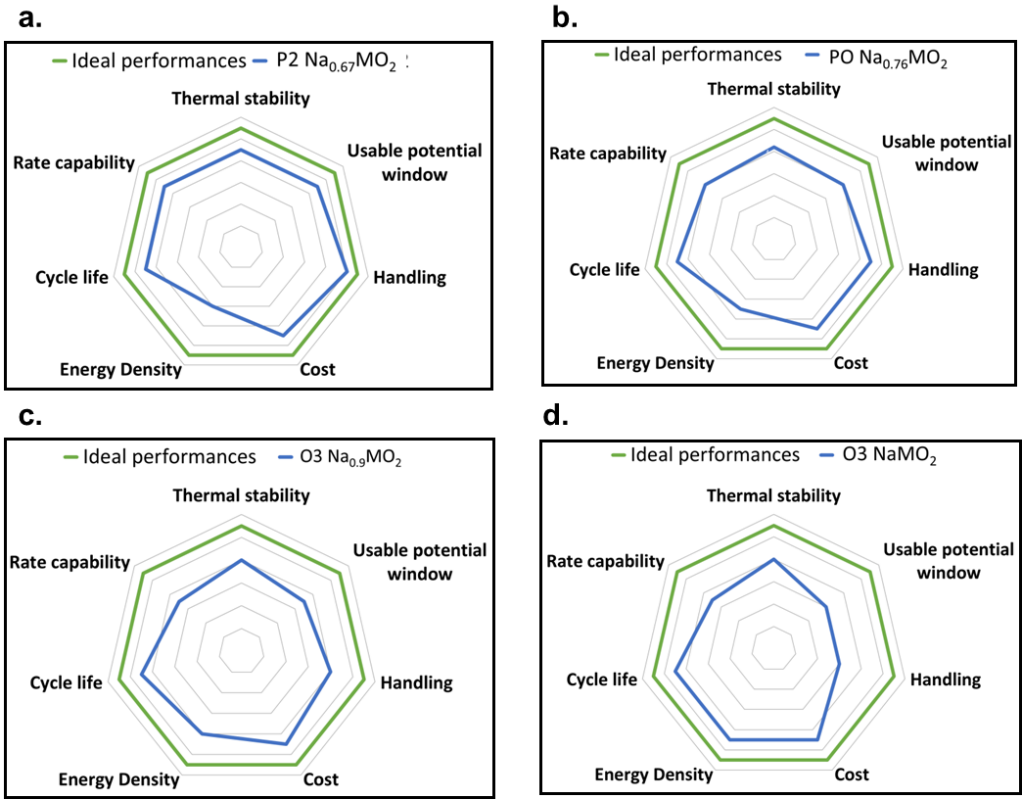

Figure 9: Performance comparison of a) P2 $Na_{0.67}MO_2$, b) PO $Na_{0.76}MO_2$, c) O3 $Na_{0.9}MO_2$ and d) O3 $NaMO_2$.

A final criterion for selecting the positive electrode material is cost, since it infers ~20 % of the overall cell components. Considering price per Wh, intuitively the P2 phase would be more expensive as more material is needed to get the same energy compared to O3 phases. However, the amount of Nickel, the most expensive component, being lesser than the O3 phase, it should counterbalance the excess of material in terms of cost and make all compounds prices equivalent. Needless to say, such a ranking can be greatly modified by considering the costs of the synthesis process or by designing layered oxides composed of the most abundant chemical elements such as Mn and Fe as is done by numerous groups worldwide provided that the electrochemical performance is maintained. [37]

CONCLUSION

In the quest to understand various figures of merit that need to be fulfilled by the sodium layered oxides for their applications in sodium ion batteries, 4 different contenders with different structural packings (P2 vs. O3) were compared using combinations of Ni, Zn, Mn and Ti. Among them, the O3 $NaNi_{0.45}Zn_{0.05}Mn_{0.4}Ti_{0.1}O_2$ is the best in terms of capacity but the worst with respect to moisture stability and electrode processing. In contrast, the P2 $Na_{0.67}Ni_{0.3}Zn_{0.03}Mn_{0.52}Ti_{0.15}O_2$ phase, because of its higher cell voltage that compensates for limited capacity energy-wise, its lesser nickel content and reduced surface reactivity hence easy processing, is the most attractive for commercial scale applications. Its implementation in 18650 Na-ion cells is currently underway. Overall, this work shows the complexity of designing new materials by exploring the composition-structure space to provide solely incremental optimization in terms of performances. This is a perfect ground on which the combined arrival of computational material screening, usage of robotics to screen many different compositions and artificial intelligence (AI) could be highly beneficial.

ACKNOWLEDGEMENT

The authors thank the RS2E Network for funding as well as the financial support of Région Nouvelle Aquitaine, of the French National Research Agency (STORE-EX Labex Project ANR-10-LABX-76-01). E.G and S. M. acknowledges Horizon 2020 research and innovation program under grant agreement No 875629- NAIMA. A.A.M. is grateful to the Russian Science Foundation (grant No. 17-73-30006) for financial support. Access to transmission electron microscopy equipment was provided by AICF of Skoltech. Use of the 11-BM mail-in service of the APS at Argonne National Laboratory was supported by the US Department of Energy under contract No. DE-AC02-06CH11357 and is gratefully acknowledged.

REFERENCES

[1] Y.-K. Sun, "Direction for Commercialization of O3-Type Layered Cathodes for Sodium-Ion Batteries," *ACS Energy Lett.*, vol. 5, no. 4, pp. 1278–1280, Apr. 2020, doi: 10.1021/acsenergylett.0c00597.

[2] J. Deng, W.-B. Luo, S.-L. Chou, H.-K. Liu, and S.-X. Dou, "Sodium-Ion Batteries: From Academic Research to Practical Commercialization," *Adv. Energy Mater.*, vol. 8, no. 4, p. 1701428, 2018, doi: 10.1002/aenm.201701428.

[3] S. Komaba *et al.*, "Electrochemical Na Insertion and Solid Electrolyte Interphase for Hard-Carbon Electrodes and Application to Na-Ion Batteries," *Adv. Funct. Mater.*, vol. 21, no. 20, pp. 3859–3867, 2011, doi: 10.1002/adfm.201100854.

[4] N. Yabuuchi, K. Kubota, M. Dahbi, and S. Komaba, "Research Development on Sodium-Ion Batteries," *Chem. Rev.*, vol. 114, no. 23, pp. 11636–11682, Dec. 2014, doi: 10.1021/cr500192f.

[5] R. Dugas, B. Zhang, P. Rozier, and J. M. Tarascon, "Optimization of Na-Ion Battery Systems Based on Polyanionic or Layered Positive Electrodes and Carbon Anodes," *J. Electrochem. Soc.*, vol. 163, no. 6, p. A867, Mar. 2016, doi: 10.1149/2.0051605jes.

[6] S. D. Shraer *et al.*, "Development of vanadium-based polyanion positive electrode active materials for high-voltage sodium-based batteries," *Nat. Commun.*, vol. 13, no. 1, Art. no. 1, Jul. 2022, doi: 10.1038/s41467-022-31768-5.

[7] K. Kubota, S. Kumakura, Y. Yoda, K. Kuroki, and S. Komaba, "Electrochemistry and Solid-State Chemistry of NaMeO2 (Me = 3d Transition Metals)," *Adv. Energy Mater.*, vol. 8, no. 17, p. 1703415, 2018, doi: 10.1002/aenm.201703415.

[8] C. Delmas, C. Fouassier, and P. Hagenmuller, "Structural classification and properties of the layered oxides," *Phys. BC*, vol. 99, no. 1, pp. 81–85, Jan. 1980, doi: 10.1016/0378-4363(80)90214-4.

[9] S. Mariyappan, Q. Wang, and J. M. Tarascon, "Will Sodium Layered Oxides Ever Be Competitive for Sodium Ion Battery Applications?," *J. Electrochem. Soc.*, vol. 165, no. 16, pp. A3714–A3722, 2018, doi: 10.1149/2.0201816jes.

[10] S. Mariyappan *et al.*, "The Role of Divalent (Zn^{2+} /Mg^{2+} /Cu^{2+}) Substituents in Achieving Full Capacity of Sodium Layered Oxides for Na-Ion Battery Applications," *Chem. Mater.*, vol. 32, no. 4, pp. 1657–1666, Feb. 2020, doi: 10.1021/acs.chemmater.9b05205.

[11] P.-F. Wang *et al.*, “Ti-Substituted NaNi0.5Mn0.5-xTixO2 Cathodes with Reversible O3−P3 Phase Transition for High-Performance Sodium-Ion Batteries,” *Adv. Mater.*, vol. 29, no. 19, p. 1700210, 2017, doi: 10.1002/adma.201700210.
[12] M. Sathiya, Q. Jacquet, M.-L. Doublet, O. M. Karakulina, J. Hadermann, and J.-M. Tarascon, “A Chemical Approach to Raise Cell Voltage and Suppress Phase Transition in O3 Sodium Layered Oxide Electrodes,” *Adv. Energy Mater.*, vol. 8, no. 11, p. 1702599, Apr. 2018, doi: 10.1002/aenm.201702599.
[13] C. Zhao *et al.*, “Rational design of layered oxide materials for sodium-ion batteries,” *Science*, vol. 370, no. 6517, pp. 708–711, Nov. 2020, doi: 10.1126/science.aay9972.
[14] J. Rodriguez-Carvajal, “FULLPROF: a program for Rietveld refinement and pattern matching analysis,” *satellite meeting on powder diffraction XV Congr. IUCr*, Toulouse, France, 1990.
[15] J. B. Leriche *et al.*, “An Electrochemical Cell for Operando Study of Lithium Batteries Using Synchrotron Radiation,” *J. Electrochem. Soc.*, vol. 157, no. 5, p. A606, Apr. 2010, doi: 10.1149/1.3355977.
[16] M. Doyle, J. Newman, and J. Reimers, “A quick method of measuring the capacity versus discharge rate for a dual lithium-ion insertion cell undergoing cycling,” *J. Power Sources*, vol. 52, no. 2, pp. 211–216, Dec. 1994, doi: 10.1016/0378-7753(94)02012-4.
[17] W. Weppner and R. A. Huggins, “Determination of the Kinetic Parameters of Mixed-Conducting Electrodes and Application to the System Li3Sb,” *J. Electrochem. Soc.*, vol. 124, no. 10, p. 1569, Oct. 1977, doi: 10.1149/1.2133112.
[18] P. Desai *et al.*, “Mastering the synergy between Na3V2(PO4)2F3 electrode and electrolyte: A must for Na-ion cells,” *Energy Storage Mater.*, vol. 57, pp. 102–117, Mar. 2023, doi: 10.1016/j.ensm.2023.02.004.
[19] G. Yan, D. Alves-Dalla-Corte, W. Yin, N. Madern, G. Gachot, and J.-M. Tarascon, “Assessment of the Electrochemical Stability of Carbonate-Based Electrolytes in Na-Ion Batteries,” *J. Electrochem. Soc.*, vol. 165, no. 7, p. A1222, Apr. 2018, doi: 10.1149/2.0311807jes.
[20] A. Rougier, P. Gravereau, and C. Delmas, “Optimization of the Composition of the Li1 − z Ni1 + z O 2 Electrode Materials: Structural, Magnetic, and Electrochemical Studies,” *J. Electrochem. Soc.*, vol. 143, no. 4, pp. 1168–1175, Apr. 1996, doi: 10.1149/1.1836614.
[21] Z. Lu and J. R. Dahn, “In Situ X-Ray Diffraction Study of P 2 - Na2 / 3 [Ni1 / 3Mn2 / 3] O 2,” *J. Electrochem. Soc.*, vol. 148, no. 11, p. A1225, Sep. 2001, doi: 10.1149/1.1407247.
[22] C. Chen *et al.*, “P2/O3 biphasic Fe/Mn-based layered oxide cathode with ultrahigh capacity and great cyclability for sodium ion batteries,” *Nano Energy*, vol. 90, p. 106504, Dec. 2021, doi: 10.1016/j.nanoen.2021.106504.
[23] B. Mortemard de Boisse, D. Carlier, M. Guignard, L. Bourgeois, and C. Delmas, “P2-Na $_x$ Mn $_{1/2}$ Fe $_{1/2}$ O $_2$ Phase Used as Positive Electrode in Na Batteries: Structural Changes Induced by the Electrochemical (De)intercalation Process,” *Inorg. Chem.*, vol. 53, no. 20, pp. 11197–11205, Oct. 2014, doi: 10.1021/ic5017802.
[24] X. Bai *et al.*, “Anionic Redox Activity in a Newly Zn-Doped Sodium Layered Oxide P2-Na2/3Mn1−yZnyO2 (0 < y < 0.23),” *Adv. Energy Mater.*, vol. 8, no. 32, p. 1802379, 2018, doi: 10.1002/aenm.201802379.
[25] Z. Cheng *et al.*, “A Rational Biphasic Tailoring Strategy Enabling High-Performance Layered Cathodes for Sodium-Ion Batteries,” *Angew. Chem. Int. Ed.*, vol. n/a, no. n/a, p. e202117728, doi: 10.1002/anie.202117728.
[26] Z. Liu, C. Zhou, J. Liu, L. Yang, J. Liu, and M. Zhu, “Phase tuning of P2/O3-type layered oxide cathode for sodium ion batteries via a simple Li/F co-doping route,” *Chem. Eng. J.*, vol. 431, p. 134273, Mar. 2022, doi: 10.1016/j.cej.2021.134273.
[27] Y.-K. Sun, D.-J. Lee, Y. J. Lee, Z. Chen, and S.-T. Myung, “Cobalt-Free Nickel Rich Layered Oxide Cathodes for Lithium-Ion Batteries,” *ACS Appl. Mater. Interfaces*, vol. 5, no. 21, pp. 11434–11440, Nov. 2013, doi: 10.1021/am403684z.

[28] E. Lee, S. Muhammad, T. Kim, H. Kim, W. Lee, and W.-S. Yoon, “Tracking the Influence of Thermal Expansion and Oxygen Vacancies on the Thermal Stability of Ni-Rich Layered Cathode Materials,” *Adv. Sci.*, vol. 7, no. 12, p. 1902413, 2020, doi: 10.1002/advs.201902413.
[29] W. Zuo *et al.*, “The stability of P2-layered sodium transition metal oxides in ambient atmospheres,” *Nat. Commun.*, vol. 11, no. 1, p. 3544, Dec. 2020, doi: 10.1038/s41467-020-17290-6.
[30] Y. You, A. Dolocan, W. Li, and A. Manthiram, “Understanding the Air-Exposure Degradation Chemistry at a Nanoscale of Layered Oxide Cathodes for Sodium-Ion Batteries,” *Nano Lett.*, vol. 19, no. 1, pp. 182–188, Jan. 2019, doi: 10.1021/acs.nanolett.8b03637.
[31] Y. Cao *et al.*, “A Water Stable, Near-Zero-Strain O3-Layered Titanium-Based Anode for Long Cycle Sodium-Ion Battery,” *Adv. Funct. Mater.*, vol. 30, no. 7, p. 1907023, 2020, doi: 10.1002/adfm.201907023.
[32] W. Zuo, Z. Xiao, M. Zarrabeitia, X. Xue, Y. Yang, and S. Passerini, “Guidelines for Air-Stable Lithium/Sodium Layered Oxide Cathodes,” *ACS Mater. Lett.*, vol. 4, no. 6, pp. 1074–1086, Jun. 2022, doi: 10.1021/acsmaterialslett.1c00827.
[33] B. S. Kumar *et al.*, “Fundamental Principles toward Designing High Na-Containing P2-Structured ‘Layered’ Na-Transition Metal Oxides as High-Performance Cathode Materials for Na-Ion Batteries,” *Chem. Mater.*, vol. 34, no. 23, pp. 10470–10483, Dec. 2022, doi: 10.1021/acs.chemmater.2c02478.
[34] C. Zhao *et al.*, “Revealing High Na-Content P2-Type Layered Oxides as Advanced Sodium-Ion Cathodes,” *J. Am. Chem. Soc.*, vol. 142, no. 12, pp. 5742–5750, Mar. 2020, doi: 10.1021/jacs.9b13572.
[35] C. Chen *et al.*, “Core–Shell Layered Oxide Cathode for High-Performance Sodium-Ion Batteries,” *ACS Appl. Mater. Interfaces*, vol. 12, no. 6, pp. 7144–7152, Feb. 2020, doi: 10.1021/acsami.9b19260.
[36] X. Liang, T.-Y. Yu, H.-H. Ryu, and Y.-K. Sun, “Hierarchical O3/P2 heterostructured cathode materials for advanced sodium-ion batteries,” *Energy Storage Mater.*, vol. 47, pp. 515–525, May 2022, doi: 10.1016/j.ensm.2022.02.043.
[37] S. Jia, J. Counsell, M. Adamič, A. Jonderian, and E. McCalla, “High-throughput design of Na–Fe–Mn–O cathodes for Na-ion batteries,” *J. Mater. Chem. A*, vol. 10, no. 1, pp. 251–265, Dec. 2021, doi: 10.1039/D1TA07940A.